Publications of the Astronomical Society of the Pacific, 136:054402 (13pp), 2024 May https://doi.org/10.1088/1538-3873/ad48b8
© 2024. The Astronomical Society of the Pacific. All rights reserved.

KMT-2023-BLG-1431Lb: A New $q < 10^{-4}$ Microlensing Planet from a Subtle Signature

Aislyn Bell[1,2], Jiyuan Zhang[3], Weicheng Zang[1], Youn Kil Jung[4,5], Jennifer C. Yee[1], Hongjing Yang[3], Takahiro Sumi[6], Andrzej Udalski[7]
(Leading Authors),
Michael D. Albrow[8], Sun-Ju Chung[4], Andrew Gould[9,10], Cheongho Han[11], Kyu-Ha Hwang[4], Yoon-Hyun Ryu[4], In-Gu Shin[1], Yossi Shvartzvald[12], Sang-Mok Cha[4,13], Dong-Jin Kim[4], Seung-Lee Kim[4], Chung-Uk Lee[4], Dong-Joo Lee[4], Yongseok Lee[4,13], Byeong-Gon Park[4,5], Richard W. Pogge[10]
(The KMTNet Collaboration),
Yunyi Tang[3], Jennie McCormick[14], Subo Dong[15,16], Zhuokai Liu[15,16], Leandro de Almeida[17], Shude Mao[3], Dan Maoz[18], Wei Zhu[3]
(The MAP & μFUN Follow-up Team),
Fumio Abe[19], Richard Barry[20], David P. Bennett[20,21], Aparna Bhattacharya[20,21], Ian A. Bond[22], Hirosane Fujii[6], Akihiko Fukui[23,24], Ryusei Hamada[6], Yuki Hirao[6], Stela Ishitani Silva[20,25], Yoshitaka Itow[19], Rintaro Kirikawa[6], Iona Kondo[6], Naoki Koshimoto[20,21], Yutaka Matsubara[19], Sho Matsumoto[6], Shota Miyazaki[6], Yasushi Muraki[19], Arisa Okamura[6], Greg Lmschenk[20], Clément Ranc[26], Nicholas J. Rattenbury[27], Yuki Satoh[6], Daisuke Suzuki[6], Taiga Toda[6], Mio Tomoyoshi[6], Paul J. Tristram[28], Aikaterini Vandorou[20,21], Hibiki Yama[6], Kansuke Yamashita[6]
(The MOA Collaboration),
and
Przemek Mróz[7], Jan Skowron[7], Radoslaw Poleski[7], Michał K. Szymański[7], Igor Soszyński[7], Paweł Pietrukowicz[7], Szymon Kozłowski[7], Krzysztof Ulaczyk[29], Krzysztof A. Rybicki[7], Patryk Iwanek[7], Marcin Wrona[7], Mariusz Gromadzki[7]
(The OGLE Collaboration)

[1] Center for Astrophysics | Harvard & Smithsonian, 60 Garden St., Cambridge, MA 02138, USA
[2] Department of Astrophysical and Planetary Sciences, University of Colorado, Boulder, CO, USA
[3] Department of Astronomy, Tsinghua University, Beijing 100084, People's Republic of China; zhangjiyuan2022@gmail.com
[4] Korea Astronomy and Space Science Institute, Daejon 34055, Republic of Korea
[5] University of Science and Technology, Korea, (UST), 217 Gajeong-ro Yuseong-gu, Daejeon 34113, Republic of Korea
[6] Department of Earth and Space Science, Graduate School of Science, Osaka University, Toyonaka, Osaka 560-0043, Japan
[7] Astronomical Observatory, University of Warsaw, Al. Ujazdowskie 4, 00-478 Warszawa, Poland
[8] University of Canterbury, Department of Physics and Astronomy, Private Bag 4800, Christchurch 8020, New Zealand
[9] Max-Planck-Institute for Astronomy, Königstuhl 17, 69117 Heidelberg, Germany
[10] Department of Astronomy, Ohio State University, 140 W. 18th Ave., Columbus, OH 43210, USA
[11] Department of Physics, Chungbuk National University, Cheongju 28644, Republic of Korea
[12] Department of Particle Physics and Astrophysics, Weizmann Institute of Science, Rehovot 76100, Israel
[13] School of Space Research, Kyung Hee University, Yongin, Kyeonggi 17104, Republic of Korea
[14] Farm Cove Observatory, Centre for Backyard Astrophysics, Pakuranga, Auckland, New Zealand
[15] Department of Astronomy, School of Physics, Peking University, Yiheyuan Rd. 5, Haidian District, Beijing 100871, People's Republic of China
[16] Kavli Institute for Astronomy and Astrophysics, Peking University, Yiheyuan Rd. 5, Haidian District, Beijing 100871, People's Republic of China
[17] Laboratório Nacional de Astrofísica, Rua Estados Unidos 154, 37504-364 Itajubá–MG, Brazil
[18] School of Physics and Astronomy, Tel-Aviv University, Tel-Aviv 6997801, Israel
[19] Institute for Space-Earth Environmental Research, Nagoya University, Nagoya 464-8601, Japan
[20] Code 667, NASA Goddard Space Flight Center, Greenbelt, MD 20771, USA
[21] Department of Astronomy, University of Maryland, College Park, MD 20742, USA
[22] Institute of Natural and Mathematical Sciences, Massey University, Auckland 0745, New Zealand
[23] Department of Earth and Planetary Science, Graduate School of Science, The University of Tokyo, 7-3-1 Hongo, Bunkyo-ku, Tokyo 113-0033, Japan
[24] Instituto de Astrofísica de Canarias, Vía Láctea s/n, E-38205 La Laguna, Tenerife, Spain
[25] Department of Physics, The Catholic University of America, Washington, DC 20064, USA
[26] Sorbonne Université, CNRS, Institut d'Astrophysique de Paris, IAP, F-75014, Paris, France
[27] Department of Physics, University of Auckland, Private Bag 92019, Auckland, New Zealand
[28] University of Canterbury Mt. John Observatory, P.O. Box 56, Lake Tekapo 8770, New Zealand
[29] Department of Physics, University of Warwick, Gibbet Hill Road, Coventry, CV4 7AL, UK
Received 2023 November 22; accepted 2024 May 8; published 2024 May 28

Abstract

The current studies of microlensing planets are limited by small number statistics. Follow-up observations of high-magnification microlensing events can efficiently form a statistical planetary sample. Since 2020, the Korea Microlensing Telescope Network (KMTNet) and the Las Cumbres Observatory (LCO) global network have been conducting a follow-up program for high-magnification KMTNet events. Here, we report the detection and analysis of a microlensing planetary event, KMT-2023-BLG-1431, for which the subtle (0.05 mag) and short-lived (5 hr) planetary signature was characterized by the follow-up from KMTNet and LCO. A binary-lens single-source (2L1S) analysis reveals a planet/host mass ratio of $q = (0.72 \pm 0.07) \times 10^{-4}$, and the single-lens binary-source (1L2S) model is excluded by $\Delta\chi^2 = 80$. A Bayesian analysis using a Galactic model yields estimates of the host star mass of $M_{\rm host} = 0.57^{+0.33}_{-0.29}\,M_\odot$, the planetary mass of $M_{\rm planet} = 13.5^{+8.1}_{-6.8}\,M_\oplus$, and the lens distance of $D_{\rm L} = 6.9^{+0.8}_{-1.7}$ kpc. The projected planet-host separation of $a_\perp = 2.3^{+0.5}_{-0.5}$ au or $a_\perp = 3.2^{+0.7}_{-0.8}$ au, subject to the close/wide degeneracy. We also find that without the follow-up data, the survey-only data cannot break the degeneracy of central/resonant caustics and the degeneracy of 2L1S/1L2S models, showing the importance of follow-up observations for current microlensing surveys.

Unified Astronomy Thesaurus concepts: Gravitational microlensing (672); Gravitational microlensing exoplanet detection (2147)

1. Introduction

Gravitational microlensing occurs when a lens star passes in front of a distant source star in an observer's line of sight (Einstein 1936). The gravitational field from the lens star will alter the path of light rays from the source star, magnifying the source. If a planet is orbiting the lens star, it may then perturb the light rays with its gravity. This appears in the data as a deviation from the expected light curve of the star. The microlensing method is most sensitive to planets around the Einstein ring because the corresponding caustics are the largest and thus the source has the highest probability of interacting with the caustic (Gould & Loeb 1992). For typical Galactic microlensing events, the physical Einstein ring radius corresponds to a few AU, so microlensing is most sensitive to planets in these orbits. The two most prolific exoplanet detection methods, the transit and the radial velocity methods, are more sensitive to planets that are close to their host star (e.g., Mayor & Queloz 1995), so microlensing is complementary to these other detection methods (Mao 2012; Gaudi 2012), especially for low mass-ratio ($q \lesssim 10^{-4}$) and wide-orbit planets.

However, microlensing is a challenging method for detecting exoplanets due to its rare and unpredictable nature. The typical microlensing event rate towards the Galactic bulge is only $\sim 10^{-6}$ (Sumi et al. 2013; Mróz et al. 2019). Planetary signals within microlensing events are also unpredictable, even rarer, and typically have a duration of one day or less (Mao & Paczynski 1991; Gould & Loeb 1992; Bennett & Rhie 1996). The difficult nature of the microlensing technique reduces the number of microlensing planets compared to the transit and the radial velocity methods, and the small number statistics lead to uncertainty in the mass-ratio function and multiplicity function. Only one statistical sample (Gould et al. 2010) contains a multi-planet system (Gaudi et al. 2008; Bennett et al. 2010). In addition, the mass-ratio distribution of planets with $\log q < -4$ is still uncertain. A study by Suzuki et al. (2016) contained 22 planet detections, but only two $q < 10^{-4}$ planets. That study found that the number of planets increases as q decreases until $q \sim 1.7 \times 10^{-4}$, below which the planetary occurrence rate drops. In order to improve our understand of these planets, it is essential to detect more $q < 10^{-4}$ planets and multi-planet systems in a statistically robust manner that enables population studies.

An efficient method of detecting microlensing planets is through follow-up observations of high-magnification events. High-magnification events are sensitive to planet detections because planets always produce a "central" caustic at the position of the lens star, and the source trajectory (by definition for a high-magnification event) passes very close to the lens star (Griest & Safizadeh 1998). This also makes them the primary channel for detecting multi-planet systems, because the perturbations from different planets occur near each other in both time and space. In fact, four (Gaudi et al. 2008; Han et al. 2013, 2022a, 2022b) out of five unambiguous multi-planet systems were detected in high-magnification events, and a fifth was detected in an event only just barely missing the magnification threshold ($A_{\rm thresh} > 25$, see below; Han et al. 2019). These events additionally have predictable peaks that are usually several magnitudes brighter than the baseline object, making them ideal candidates for follow-up observations. For example, the second microlensing planet, OGLE-2005-BLG-071Lb (Udalski et al. 2005; Dong et al. 2009), was detected by follow-up observations to high-magnification events. In addition, the first measurement of the microlensing planetary frequency was from a follow-up network called the Microlensing Follow Up Network (μFUN) for high-magnification events (Gould et al. 2010).

Since the commissioning of the Korean Microlensing Telescope Network (KMTNet, Kim et al. 2016), microlensing planet detections have been increasingly dominated by detections in the survey data,[30] because KMTNet can provide high-cadence multi-site observations to capture the short and weak planetary signals, with about 30 unambiguous planets every year (Jung et al. 2023). However, previous work on high-magnification events (e.g., Gould et al. 2010; Yee et al. 2012, 2013) has suggested that there can be a higher threshold for planet detections in such events because the data characterizing the planet anomalies can overlap with the data that characterizes the underlying event. Hence, even with high-cadence survey data, high-magnification events can benefit from additional monitoring.

Since 2020 July, the Microlensing Astronomy Probe (MAP[31]) collaboration has been using the Las Cumbres Observatory global network (LCO) to systematically conduct follow-up observations of high-magnification microlensing events (Brown et al. 2013). In addition to LCO, this program also uses μFUN and KMTNet to take follow-up observations. The KMTNet AlertFinder system supports this project by releasing new microlensing events every working day and updating the photometry every three hours (Kim et al. 2018b). This event-alert system, combined with the HighMagFinder system (Yang et al. 2022), identifies high-magnification events before they reach the magnification threshold of $A_{\rm thresh} = 25$ for follow-up.[32] The data from this follow-up project has been used in the papers of nine planets (Zang et al. 2021a, 2023; Yang et al. 2022; Olmschenk et al. 2023; Han et al. 2023a, 2023b, 2022c). Among them, KMT-2020-BLG-0414Lb has the lowest mass ratio ($q = (0.9\text{–}1.2) \times 10^{-5}$) of the microlensing planets detected thus far. In 2023, we continue our follow-up project and detected another low-q planet, KMT-2023-BLG-1431Lb, which has a mass ratio of $q = (0.72 \pm 0.07) \times 10^{-4}$.

The paper is structured as follows. In Section 2 we introduce the survey and follow-up observations for this event. In Section 3, we present the binary-lens single-source (2L1S) and single-lens binary source (1L2S) analysis. In Section 4, we conduct a color–magnitude diagram (CMD) analysis and a Bayesian analysis to estimate the lens physical parameters. Finally, we investigate the results only using the survey data and discuss the implications of this work in Section 5.

[30] the NASA Exoplanet Archive http://exoplanetarchive.ipac.caltech.edu.

[31] http://i.astro.tsinghua.edu.cn/~smao/MAP/

[32] Although early follow-up work used a threshold $A_{\rm thresh} = 100$, this limit was partially due to limitations in observing resources. Work by Abe et al. (2013) and Yee et al. (2021) has shown that $A_{\rm thresh} = 25$ is better for capturing the maximum sensitivity of this class of events, although it requires observing more events for a longer duration.

2. Observations and Data Reduction

2.1. Survey Observations

On 2023 June 27 (HJD′ = 10122.5, HJD′ = HJD−2450000), KMT-2023-BLG-1431 was flagged as a clear microlensing event by the KMTNet AlertFinder system (Kim et al. 2018b). The event lies in the KMTNet BLG04 field and is located at equatorial coordinates of $(\alpha, \delta)_{\rm J2000} = (18{:}04{:}44.05, -29{:}44{:}38.11)$ and Galactic coordinates of $(\ell, b) = (-1^\circ.40, -4^\circ.00)$, with a cadence of $1.0\,{\rm hr}^{-1}$ (Kim et al. 2018a). KMT-2023-BLG-1431 was later found by the Microlensing Observations in Astrophysics (MOA, Sako et al. 2008) group as MOA-2023-BLG-291 on 2023 July 5 (Bond et al. 2001) and by the Optical Gravitational Lensing Experiment (OGLE, Udalski et al. 2015) group as OGLE-2023-BLG-0879 on 2023 July 7. The cadence for the MOA and the OGLE surveys are $\sim 0.7\,{\rm hr}^{-1}$, and 0.5–1.0 night^{-1}, respectively.

KMTNet consists of three identical telescopes in the southern hemisphere: the Cerro Tololo Inter-American Observatory (CTIO) in Chile (KMTC), the South African Astronomical Observatory (SAAO) in South Africa (KMTS), and the Siding Spring Observatory (SSO) in Australia (KMTA). The KMTNet telescope is 1.6 m and equipped with 4 deg^2 cameras. The MOA group conducted a microlensing survey using a 1.8 m telescope equipped with a 2.2 deg^2 FoV camera at the Mt. John University Observatory in New Zealand. The OGLE data were acquired using the 1.3 m Warsaw Telescope with a 1.4 deg^2 FoV camera at the Las Campanas Observatory in Chile. Most KMTNet and OGLE observations were made in the I band due to its high signal-to-noise ratio for the extincted Bulge fields. A subset of observations in the V band were taken to measure the source color. The MOA images were mainly taken in the MOA-Red band, which is roughly the sum of the standard Cousins R and I band.

2.2. Follow-up Observations

At HJD′ = 10129.4, i.e., nine days before the highest magnification, the KMTNet HighMagFinder system found that this event is a candidate high-magnification event. Following the alert, the LCO, KMTNet, and μFUN groups conducted follow-up observations. For LCO, the high-cadence follow-up observations began at HJD′ = 10137.4. From HJD′ = 10138.2 to 10139.2, the KMTNet used "auto-followup" to increase the cadence of observations for BLG04 by replacing the BLG41 observations ($\Gamma = 1.5\,{\rm hr}^{-1}$ for KMTS and KMTA, and $\Gamma = 2.0\,{\rm hr}^{-1}$ for KMTC) with BLG04. The μFUN group took follow-up observations from a 0.18 m Newtonian telescope at El Sauce Observatory in Chile (CHI-18), the Farm Cove Observatory (FCO) in New Zealand and a 0.6 m telescope at Observatorio do Pico dos Dias (OPD) in Brazil.

Table 1
Data Information with Corresponding Data Reduction Method

Collaboration	Site	Name	Filter	$N_{\rm data}$	Reduction Method	$(k, e_{\rm min})$[a]
KMTNet	SSO	KMTA04	*I*	398	pySIS[b]	(1.12, 0.004)
KMTNet	CTIO	KMTC04	*I*	664	pySIS	(1.10, 0.004)
KMTNet	CTIO	KMTC04 (*V*)[c]	*V*	65	pySIS	...
KMTNet	SAAO	KMTS04	*I*	377	pySIS	(1.04, 0.008)
MOA	Mt. John Observatory	MOA	Red	570	Bond et al. (2001)	(1.45, 0.006)
OGLE	Las Campanas Observatory	OGLE	*I*	197	Wozniak (2000)	(1.83, 0.003)
MAP	SSO	LCOA	*I*	115	pySIS	(1.19, 0.002)
MAP	CTIO	LCOC	*I*	109	pySIS	(0.77, 0.005)
MAP	SAAO	LCOS	*I*	143	pySIS	(0.87, 0.004)
μFUN	Farm Cove Observatory	FCO	unfiltered	45	pySIS	(0.46, 0.000)
μFUN	El Sauce Observatory	CHI-18[d]	580–700 nm	...	pySIS	...
μFUN	Observatorio do Pico dos Dias	OPD[d]	*I*	...	pySIS	...

Notes.
[a] $(k, e_{\rm min})$ are the error renormalization factors as described in Yee et al. (2012).
[b] Albrow et al. (2009), Yang et al. (2024).
[c] Only used for the color measurement of the source star.
[d] Not included in the analysis due to no coverage on the anomaly.

2.3. Data Reduction

The data used in the light-curve analysis were reduced by the difference image analysis (DIA, Tomaney & Crotts 1996; Alard & Lupton 1998) pipelines: pySIS (Albrow et al. 2009; Yang et al. 2024) for KMTNet, LCO, and μFUN; Bond et al. (2001) for MOA; and Wozniak (2000) for OGLE. Ultimately, the CHI-18 and OPD data were taken after the anomaly, so they were not used in the analysis. The *I*-band magnitude of the data has been calibrated to the standard *I*-band magnitude using the OGLE-III star catalog (Szymański et al. 2011). The errors from the DIA pipelines were re-normalized using the method of Yee et al. (2012), which enables χ^2/dof for each data set to become unity, where "dof" is the number of degrees of freedom. Table 1 summarizes the reduction method, the error renormalization factors for each data set.

3. Light-curve Analysis

Figure 1 displays the observed data together with the best-fit single-lens single-source (1L1S, Paczyński 1986) model. There is a 0.2 day bump 0.45 day before the peak of the 1L1S model. This anomaly is covered by multiple sites (KMTA04, KMTS04, LOCA, and LCOS) making it very secure. Because such a short-lived bump can be caused by both a binary-lens single-source (2L1S) model and a single-lens binary-source (1L2S) model, we conduct both 2L1S and 1L2S analysis below.

3.1. Binary-lens Single-source Analysis

A static 2L1S model requires seven parameters to calculate the magnification, $A(t)$, at any given time. The first three are (t_0, u_0, $t_{\rm E}$), i.e., the time at which the source passes closest to the center of lens mass, t_0, the impact parameter of this approach normalized by the angular Einstein radius $\theta_{\rm E}$, u_0, and the Einstein radius crossing time,

$$t_{\rm E} = \frac{\theta_{\rm E}}{\mu_{\rm rel}}; \qquad \theta_{\rm E} = \sqrt{\kappa M_{\rm L} \pi_{\rm rel}}, \tag{1}$$

where $\kappa \equiv \frac{4G}{c^2 {\rm au}} \simeq 8.144 \frac{\rm mas}{M_\odot}$, $M_{\rm L}$ is the lens mass, and ($\pi_{\rm rel}$, $\mu_{\rm rel}$) are the lens-source relative (parallax, proper motion). The next three (q, s, α) define the binary geometry: the binary mass ratio, q, the projected separation between the binary components normalized to the Einstein radius, s, and the angle between the source trajectory and the binary axis, α. The last parameter, ρ, is the angular source radius θ_* normalized by the angular Einstein radius, i.e., $\rho = \theta_*/\theta_{\rm E}$. In addition, for each data set i, we introduce two flux parameters $f_{{\rm S},i}$ and $f_{{\rm B},i}$, representing the flux of the source star and any blended flux. Then, the observed flux, $f_i(t)$, is

$$f_i(t) = f_{{\rm S},i} A(t) + f_{{\rm B},i}, \tag{2}$$

where $A(t)$ is calculated by the advanced contour integration code (Bozza 2010; Bozza et al. 2018) `VBBinaryLensing`.[33] We also consider the brightness profile of the source star by adopting a linear limb-darkening law (An et al. 2002; Claret & Bloemen 2011).

To locate the local χ^2 minima, we first conduct a two-step grid search over the parameter plane ($\log s$, $\log q$, $\log \rho$, α). In the first step, a sparse grid search consists 61 values evenly distributed in $-1.5 \leqslant \log s \leqslant 1.5$, 61 values evenly distributed in $-6 \leqslant \log q \leqslant 0$, nine values evenly distributed in $-4.0 \leqslant \log \rho \leqslant -1.6$, and 16 values evenly distributed in

[33] http://www.fisica.unisa.it/GravitationAstrophysics/VBBinaryLensing.htm

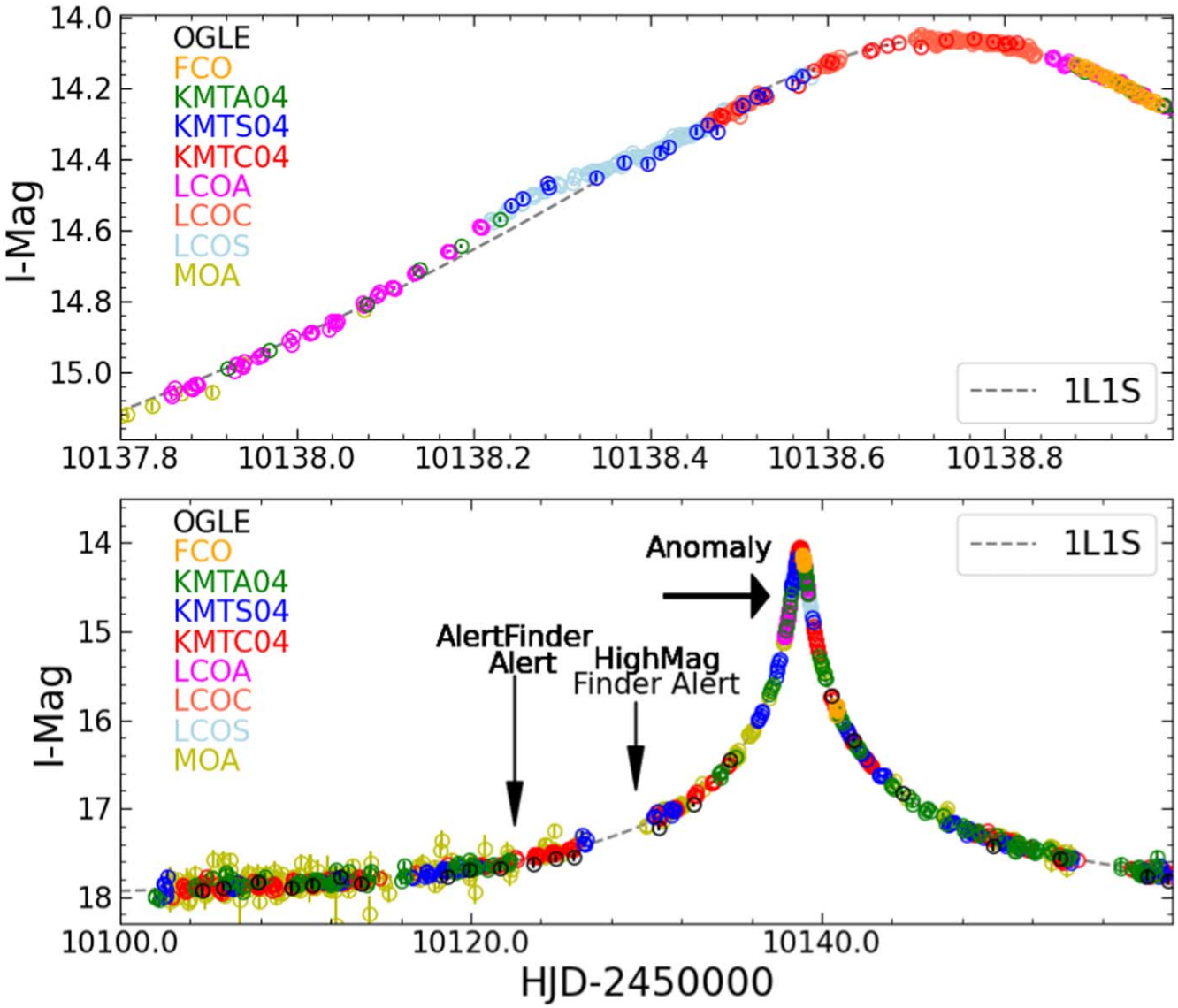

Figure 1. Light curve of KMT-2023-BLG-1431. Upper: The event was identified as high-magnification well before the peak, leading to dense observational coverage. Lower: There is a clear deviation from a PSPL light curve (gray dashed line).

$0° \leqslant \alpha < 360°$. We find the local minima by the Markov Chain Monte Carlo (MCMC) χ^2 minimization using the `emcee` ensemble sampler (Goodman & Weare 2010; Foreman-Mackey et al. 2013), with 1500 steps for burn-in and 500 steps for sampling. Here we have tried a downhill approach[34] but found that some grids cannot evolve to local minima. We fix $\log q$, $\log s$, and $\log \rho$ and let the other four parameters (t_0, u_0, t_E, α) vary. We assume a Gaussian distribution for the noise of the photometric data and adopt uniform priors for the fitting parameters (t_0, u_0, t_E, α). As shown in the upper panel of Figure 2, the minima are contained in the region $-0.15 \leqslant \log s \leqslant 0.15$ and $-5.0 \leqslant \log q \leqslant -3.5$. In the second step, we thus conduct a denser grid search with 151 values equally spaced between $-0.15 \leqslant \log s \leqslant 0.15$, 31 values equally spaced between $-5.0 \leqslant \log q \leqslant -3.5$, seven values evenly distributed in $-3.5 \leqslant \log \rho \leqslant -2.3$, and 16 initial values evenly distributed in $0° \leqslant \alpha < 360°$. As shown in the lower panel of Figure 2, there are four distinct local minima, of which two have central caustics and two have resonant caustics. This topology follows the topology of the "central-resonant" caustic degeneracy, which was first systematically identified in 2021 KMTNet season (Ryu et al. 2022; Yang et al.

[34] We use a function based on the Nelder-Mead simplex algorithm from the SciPy package. See https://docs.scipy.org/doc/scipy/reference/generated/scipy.optimize.fmin.html#scipy.optimize.fmin.

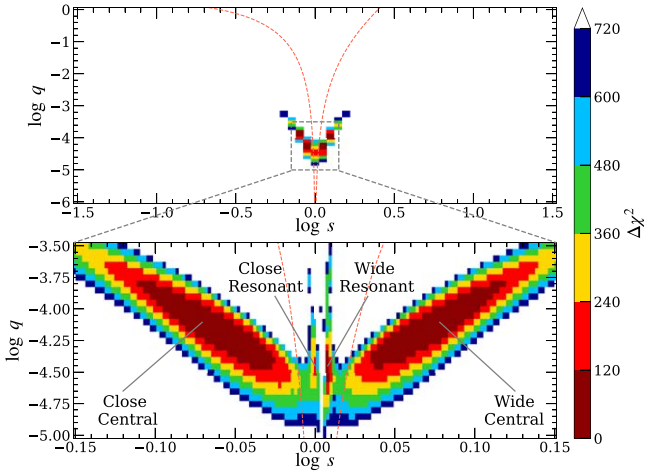

Figure 2. χ^2 surface in the ($\log s$, $\log q$) plane drawn from the grid search. The upper panel displays the space that is equally divided on a (61×61) grid with ranges of $-1.5 \leqslant \log s \leqslant 1.5$ and $-6.0 \leqslant \log q \leqslant 0$, respectively. The lower panel shows the space that is equally divided on a (151×31) grid with ranges of $-0.15 \leqslant \log s \leqslant 0.15$ and $-5.0 \leqslant \log q \leqslant -3.5$, respectively. Grid with $\Delta\chi^2 > 720$ are marked as blank. The labels "Close Central," "Wide Central," "Close Resonant," and "Wide Resonant" in the lower panel indicate four local minima. The two red dashed lines represent the boundaries between resonant and non-resonant caustics applying Equation (59) of Dominik (1999).

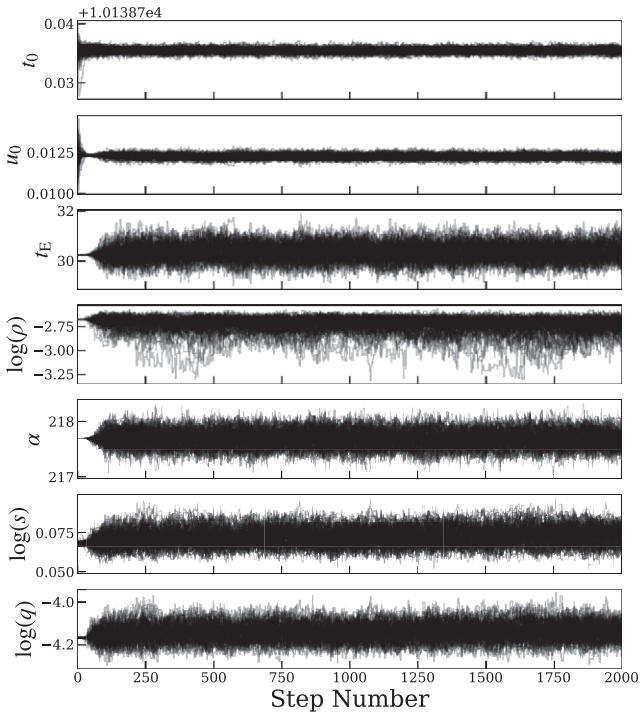

Figure 3. The positions of each walker as a function of the number of steps in the MCMC chain for the "Wide Central" model. The walkers start around the initial values and then wander and start exploring the full posterior distribution after about 150 steps.

2022; Shin et al. 2023). We label the four solutions as "Close Central," "Wide Central," "Close Resonant," and "Wide Resonant," respectively.

With all free parameters, we then investigate each local minimum by a downhill approach to search for the minimum χ^2 and by the MCMC to explore the parameter uncertainties. For the MCMC process, we adopt 100 walkers. For all models, a check on the positions of each walker as a function of steps and the auto-correlation length shows that the sample is well "burnt-in" by about 150 steps and then the parameters wander and start exploring the full posterior distribution. As an example, Figure 3 shows the positions of each walker as a function of steps for the best-fit model. We conservatively discard the first 500 steps and adopt a sample of 1500 steps to investigate the parameter distributions. Here we adopt uniform priors for (t_0, u_0, $t_{\rm E}$, $\log\rho$, α, $\log s$, $\log q$). Table 2 presents the resulting parameters. Figure 4 displays the caustic geometries and Figure 5 shows a close-up of the anomalies together with the model curves. The "Wide Central" solution provides the best fit to the observed data, and the "Close Central," "Close Resonant," and "Wide Resonant" solutions are disfavored by $\Delta\chi^2 = 0.7$, 203, and 33, respectively. The "Close Resonant" shows significant residuals to the data within the anomaly, so we exclude it. The "Wide Resonant" solution does not fit the beginning or the end of anomaly well, and the χ^2 difference is supported consistently by multiple data sets (LCOA, LCOS and KMTA), so we also rule out this solution. Hence, we only consider the two "Central" solutions in further analysis.

We note that, in contrast with other cases of the central-resonant degeneracy, (e.g., KMT-2021-BLG-0171, Yang et al. 2022), for KMT-2023-BLG-1431, the two "Resonant" solutions are not degenerate with each other. In the present case, the "Close Resonant" solution is disfavored by $\Delta\chi^2 = 170$ compared to the "Wide Resonant" solution. Figure 5 shows a close-up of the planetary signal, from which we find that the main difference between the two "Resonant" solutions is at the beginning of the anomaly. That is, the "Close Resonant" solution shows a slight dip prior to the caustic crossing, while the "Wide Resonant" solution exhibits a smooth light curve.

In addition, although the two "Central" solutions have no caustic crossings and the separation between the central caustic and the source is about eight times the source radius during the anomaly, ρ is still measured and favored over a point-source model by $\Delta\chi^2 > 15$. This is similar to the central-caustic solution of OGLE-2016-BLG-1195 (Shvartzvald et al. 2017; Bond et al. 2017; Gould et al. 2023), for which ρ was measured (6% uncertainty) with a separation of 16 times the source radius.

We also check the microlensing parallax effect (Gould 1992, 2000) by adding two parameters, ($\pi_{\rm E,N}$, $\pi_{\rm E,E}$), which are the North and East components of the microlensing parallax vector. We find a χ^2 improvement of 25 compared to the non-parallax model.

Table 2
Lensing Parameters for KMT-2023-BLG-1431 with the Survey and Follow-up Data

Parameters	2L1S				1L2S
	Central		Resonant		
	Close	Wide	Close	Wide	
χ^2/dof	2591.6/2595	2590.9/2595	2793.8/2595	2623.8/2595	2670.2/2595
$t_{0,1} - 10138$ (HJD′)	0.736 ± 0.001	0.735 ± 0.001	0.736 ± 0.001	0.736 ± 0.001	0.745 ± 0.001
$t_{0,2} - 10138$ (HJD′)	...	...	...	...	0.262 ± 0.002
$u_{0,1}(10^{-2})$	1.23 ± 0.02	1.23 ± 0.02	1.24 ± 0.02	1.25 ± 0.02	1.21 ± 0.01
$u_{0,2}(10^{-2})$	...	...	...	...	0.05 ± 0.07
$t_{\rm E}$ (days)	30.3 ± 0.3	30.4 ± 0.3	30.3 ± 0.3	30.0 ± 0.3	30.9 ± 0.3
$\rho_1(10^{-3})$	1.95 ± 0.30	1.86 ± 0.38	3.13 ± 0.07	2.77 ± 0.10	...
$\rho_2(10^{-3})$	...	...	...	...	2.87 ± 0.13
α (degree)	217.65 ± 0.16	217.69 ± 0.16	217.81 ± 0.13	218.00 ± 0.15	...
s	0.864 ± 0.012	1.184 ± 0.018	0.999 ± 0.001	1.018 ± 0.001	...
$q(10^{-4})$	0.719 ± 0.069	0.729 ± 0.073	0.344 ± 0.016	0.335 ± 0.012	...
$\log q$	-4.145 ± 0.041	-4.140 ± 0.043	-4.464 ± 0.020	-4.475 ± 0.016	...
$q_{f,I}(10^{-3})$	...	...	...	...	6.21 ± 0.49
$I_{\rm S,OGLE}$	18.748 ± 0.014	18.749 ± 0.014	18.746 ± 0.014	18.736 ± 0.014	18.771 ± 0.013

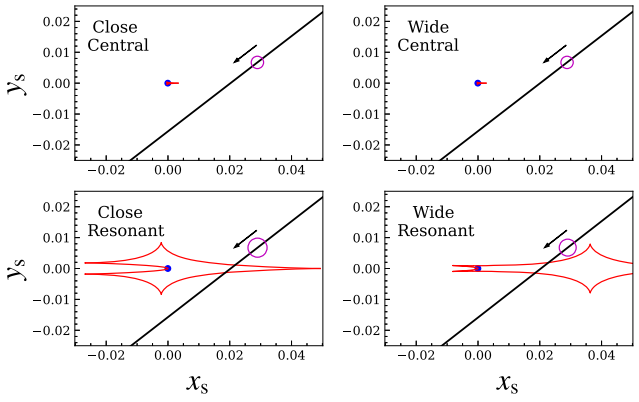

Figure 4. Geometries of the four 2L1S solutions. In each panel, the black line with an arrow represents the source trajectory with respect to the host star that is marked by blue dot, the red lines show the caustic structure, the axes are in units of the Einstein radius $\theta_{\rm E}$, and the magenta circle indicates the source radii.

However, the parallax value, 1.8 ± 0.4, is of low probability while the typical parallax value is $\sim$0.1. In addition, among the survey data, only the KMTC04 and KMTS04 data show χ^2 improvement, while the OGLE and MOA data have worse χ^2. Thus, the suspicious parallax signal is due to systematics in the KMTC04 and KMTS04 data and we adopt the models without the microlensing parallax effect.

3.2. Single-lens Binary-source Analysis

Gaudi (1998) suggested that a 1L2S model can also produce a short-lived bump-type anomaly if the second source is much fainter and passes closer to the host star. The total magnification $A_\lambda(t)$ for a waveband λ is the superposition of the 1L1S magnification of two sources and can be expressed as (Hwang et al. 2013)

$$A_\lambda(t) = \frac{A_1(t) f_{1,\lambda} + A_2(t) f_{2,\lambda}}{f_{1,\lambda} + f_{2,\lambda}} = \frac{A_1(t) + q_{f,\lambda} A_2(t)}{1 + q_{f,\lambda}}, \quad (3)$$

$$q_{f,\lambda} = \frac{f_{2,\lambda}}{f_{1,\lambda}}, \quad (4)$$

where $f_{j,\lambda}$ and $A_j(t)$ ($j = 1, 2$) are the flux at waveband λ and magnification of the two sources, respectively.

We explore the best-fit 1L2S model using the downhill approach and the MCMC, and the resulting parameters are given in Table 2. The 1L2S model is disfavored by $\Delta\chi^2 \sim 80$ compared to the best-fit 2L1S model. From Figure 5, we find that the χ^2 difference comes mainly from the anomaly, rather than some other source, reinforcing the conclusion that the 1L2S model is a poor fit to the anomaly. In addition, the putative source companion is 5.5 mag fainter than the primary source. According to Section 4, the putative secondary source would have an absolute magnitude of $M_{I,2} \sim 9.1$ mag, corresponding to an angular source radius of $\theta_{*,2} \sim 0.2\,\mu$ as. Then, the lens-source relative proper motion would be $\mu_{\rm rel} = \theta_{*,2}/\rho_2/t_{\rm E} \sim 0.8$ mas yr^{-1}. Using Equation (9) of Jung et al. (2022), which is based on the study of the $\mu_{\rm rel}$ distribution of observed planetary microlensing events (Gould 2022), the probability of $\mu_{\rm rel} \leqslant 0.8$ mas yr^{-1} is only 0.018. Hence, based on both the $\Delta\chi^2$ and the low $\mu_{\rm rel}$, we exclude the 1L2S model.

4. Physical Parameters

4.1. Color-Magnitude Diagram (CMD)

The 2L1S light-curve analysis yields a measurement of ρ, which, combined with the angular source radius θ_*, can be used to calculate the angular Einstein radius: $\theta_{\rm E} = \theta_*/\rho$. We

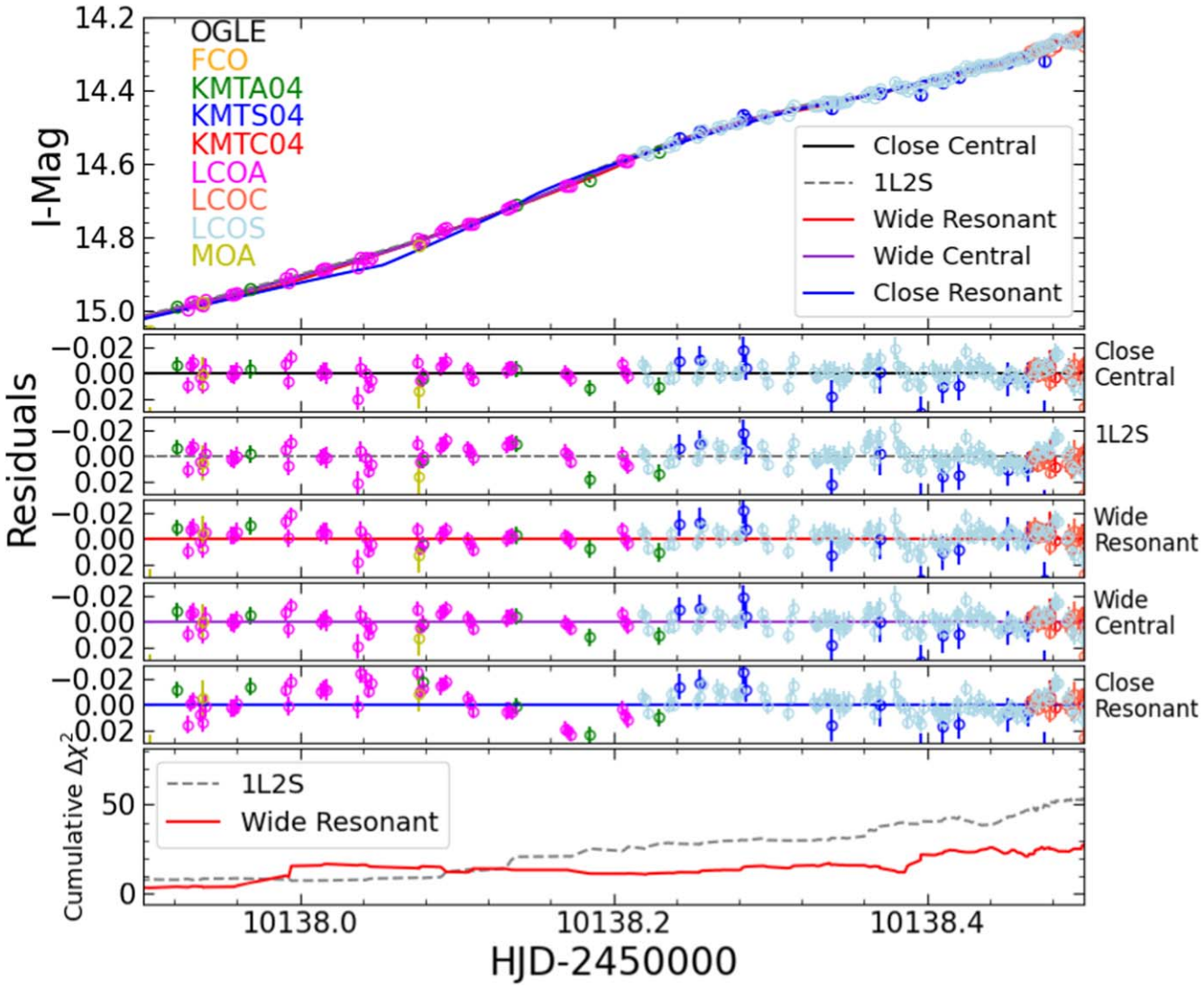

Figure 5. Detailed comparison of the disfavored model fits to the anomaly: "Close Central," "Wide Central," "Close Resonant" "Wide Resonant," and "1L2S." The top panel shows the models plotted with the data, while the middle panels show the residuals to the models. The "Close Resonant" models shows clear residuals and is ruled out. The deviations in the "Wide Resonant" and "1L2S" models are more subtle but (as shown in the bottom panel), amount to $\Delta\chi^2$ differences of ∼30 and ∼80, respectively, over the course of the anomaly. The "Close Central" model is competitive with the best-fit "Wide Central" model.

estimate θ_* by locating the source on a $V-I$ versus I CMD (Figure 6) using the OGLE-III ambient stars (Szymański et al. 2011) within 120″ of the event. The centroid of the red giant clump in this field is measured to be $(V-I, I)_{\rm cl} = (1.76 \pm 0.01, 15.18 \pm 0.02)$. From Bensby et al. (2013) and Table 1 of Nataf et al. (2013), we estimate the de-reddened color and magnitude of the red giant clump to be $(V-I,\ I)_{\rm cl,0} = (1.06 \pm 0.03, 14.39 \pm 0.04)$.

The color and brightness of the source star are measured from the KMTC04 data and converted to the OGLE-III system by matching their respective star catalogs. From the light-curve analysis, the source brightness is $I_{\rm S} = 18.75 \pm 0.01$. Because each KMTC04 V-band data point was taken one minute around one KMTC04 I-band data point, we derive the source color by regression of each pair of KMTC04 V versus I data points and obtain $(V-I)_{\rm S} = 1.76 \pm 0.01$.

The offsets of these values from the observed red clump leads to the source de-reddened color and magnitude of $(V-I, I)_{\rm S,0} = (0.68 \pm 0.03,\ 17.96 \pm 0.05)$. According to Bessell & Brett (1988), the source star is probably a G-type dwarf or subgiant. Applying the color/surface-brightness relation for dwarfs and subgiants of Adams et al. (2018), we obtain the angular source radius of

$$\theta_* = 0.805 \pm 0.040\ \mu{\rm as}. \quad (5)$$

We summarize the CMD parameters and the resulting $\theta_{\rm E}$ and $\mu_{\rm rel}$ for the two "Central" solutions in Table 3.

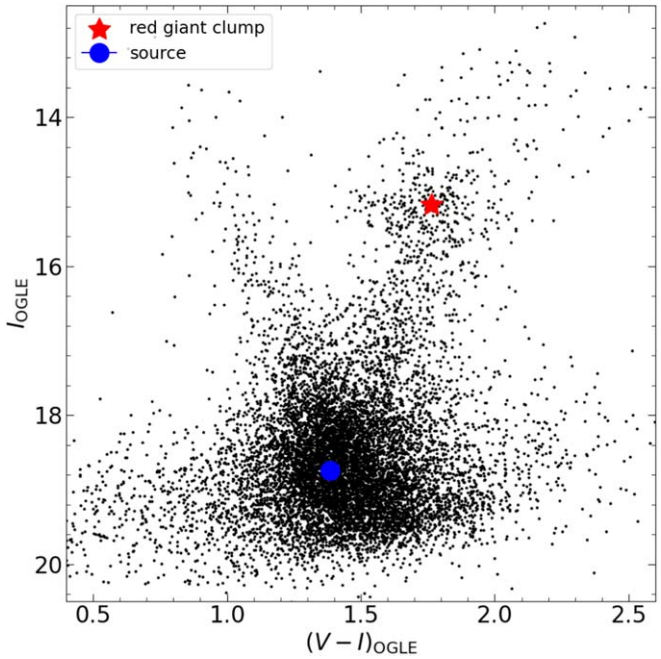

Figure 6. The the OGLE-III CMD for KMT-2023-BLG-1431, constructed using the field stars within 120″ centered the source star. The red star indicates the centroid of the red giant clump, and the blue dot shows the position of the source star.

Table 3
CMD Parameters and Derived θ_E and μ_{rel} for KMT-2023-BLG-1431

Red Clump:		
$(V-I)_{cl}$	1.76 ± 0.01	
I_{cl}	15.18 ± 0.02	
$(V-I)_{cl,\,0}$	1.06 ± 0.03	
$I_{cl,\,0}$	14.39 ± 0.04	
	Close Central	Wide Central
Source:		
$(V-I)_S$	1.76 ± 0.01	←
I_S	18.748 ± 0.014	18.749 ± 0.014
$(V-I)_{S,0}$	0.68 ± 0.03	←
$I_{S,0}$	17.96 ± 0.05	17.96 ± 0.05
θ_* (μas)	0.805 ± 0.040	0.805 ± 0.040
Event:		
θ_E (mas)	0.413 ± 0.067	0.433 ± 0.090
μ_{rel} (mas yr^{-1})	4.98 ± 0.81	5.20 ± 1.08

4.2. Galactic-model Analysis

With the angular Einstein radius θ_E and the microlensing parallax π_E, the lens mass, M_L, and the lens distance, D_L, can be uniquely determined by Gould (1992, 2000)

$$M_L = \frac{\theta_E}{\kappa \pi_E}; \qquad D_L = \frac{\mathrm{au}}{\pi_E \theta_E + \pi_S}, \tag{6}$$

where π_S is the source parallax. For the present case, θ_E is measured but π_E is not constraint, so we estimate the physical parameters of the lens system by a Bayesian analysis based on a Galactic model.

The Galactic model is the same as used in Zhang et al. (2023), in which we adopt initial mass function from Kroupa (2001), with a $1.3M_\odot$ and $1.1M_\odot$ cutoff for the disk and the bulge lenses, respectively (Zhu et al. 2017), the stellar number density profile is depicted in Yang et al. (2021), and the dynamical distributions of the bulge and disk lenses are described by the Zhu et al. (2017) and Yang et al. (2021) model, respectively.

We generate a sample of 10^7 simulated events from prior functions of the Galactic model above by conducting a Monte Carlo simulation. For each simulated event i of solution k with parameters $t_{E,i,k}$, $\mu_{rel,i,k}$, and $\theta_{E,i,k}$, we weight it by

$$w_i = \Gamma_{i,k} \times p(t_{E,i,k}) p(\theta_{E,i,k}), \tag{7}$$

where $\Gamma_{i,k} = \theta_{E,i,k} \times \mu_{rel,i,k}$ is the microlensing event rate, and $p(t_{E,i,k})$ and $p(\theta_{E,i,k})$ are the likelihood of $t_{E,i,k}$ and $\theta_{E,i,k}$, i.e.,

$$p(t_{E,i,k}) = \frac{\exp[-(t_{E,i,k} - t_{E,k})^2 / 2\sigma^2_{t_{E,k}}]}{\sqrt{2\pi}\,\sigma_{t_{E,k}}},$$
$$p(\theta_{E,i,k}) = \frac{\exp[-(\theta_{E,i,k} - \theta_{E,k})^2 / 2\sigma^2_{\theta_{E,k}}]}{\sqrt{2\pi}\,\sigma_{\theta_{E,k}}}, \tag{8}$$

where $(\sigma_{t_{E,k}}, \sigma_{\theta_{E,k}})$ are the standard deviations of $t_{E,k}$ and $\theta_{E,k}$, respectively. $(t_{E,k}, \sigma_{t_{E,k}})$ and $(\theta_{E,k}, \sigma_{\theta_{E,k}})$ are adopted from Tables 2 and 3, respectively.

Table 4 and Figure 7 present the resulting posterior distributions of the host mass, M_{host}, the planet mass, M_{planet}, the lens distance, D_L, the lens-source relative proper motion in the heliocentric frame, $\mu_{hel,rel}$, the projected planet-host separation, $r_\perp$, derived by $sD_L\theta_E$, and the probability of a bulge lens, P_{bluge}. The values in Table 4 are the median values of the posterior distributions and the lower and upper limits determined as 16% and 84% of the distributions, respectively. It is estimated that the host star prefers an M or K dwarf located in the Galactic bulge. The median mass of the planet is the sub-Neptune mass, while the super-Earth mass and super-Neptune mass are both within 1σ.

5. Discussion: The Role of the Follow-up Data

The goal of our follow-up program is to increase the number of planet detections in high-magnification events. This was a case in which the HighMagFinder alerted the event early enough to enable dense observations over the peak, leading to the detection and characterization of a sub-Neptune mass planet. We now consider what would have happened in the absence of our follow-up program.

KMT-2023-BLG-1431 lies in KMTNet field BLG04 and so would normally be monitored at a rate of one observation per hour by KMTNet as well as being observed as part of the regular survey operations of OGLE and MOA. To evaluate the

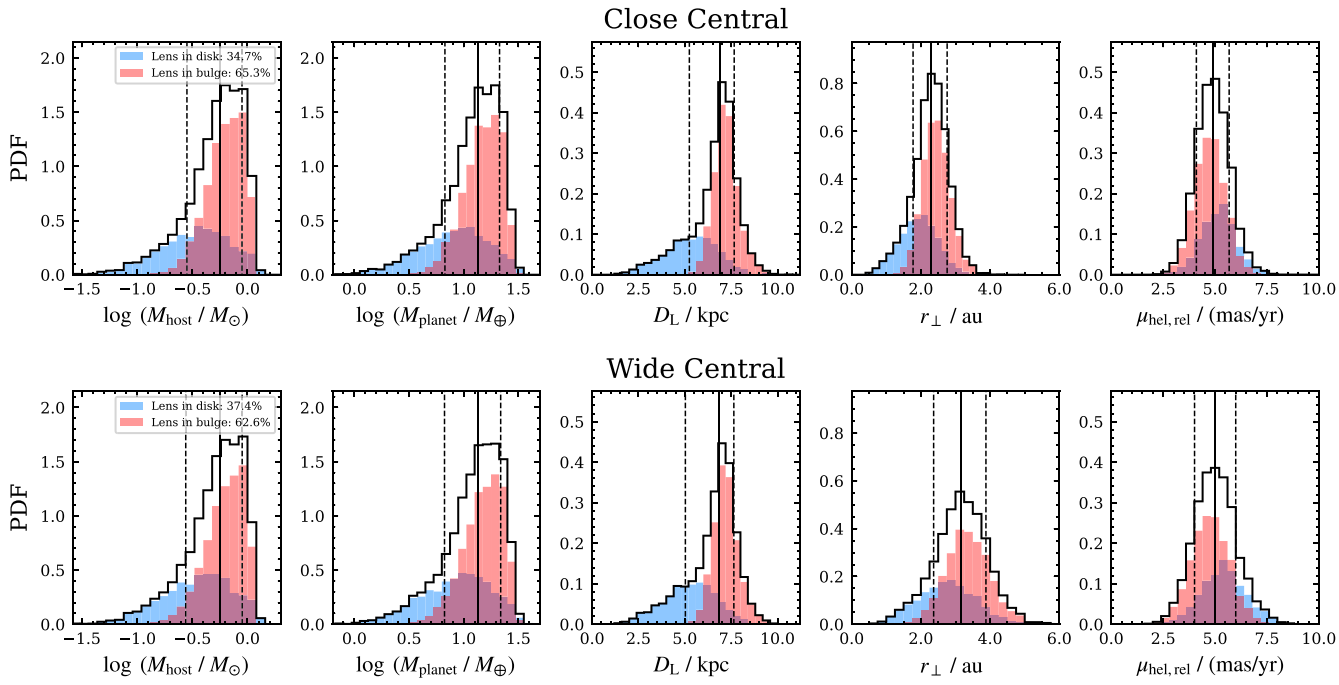

Figure 7. Bayesian posterior distributions for the lens physical parameters of KMT-2023-BLG-1431. In each panel, the black solid line and the two black dashed lines represent the median value and the 16% and 84% percentages of the distribution. Red and blue indicate the distributions for the bulge and disk lenses, respectively.

Table 4
Physical Parameters for KMT-2023-BLG-1431

Solution	Physical Properties					
	M_{host} ($M_\odot$)	M_{planet} ($M_\oplus$)	D_L (kpc)	$r_\perp$ (au)	$\mu_{hel,rel}$ (mas yr^{-1})	P_{bulge}
Close Central	$0.57^{+0.32}_{-0.28}$	$13.4^{+7.9}_{-6.7}$	$6.9^{+0.8}_{-1.6}$	$2.3^{+0.5}_{-0.5}$	$4.9^{+0.8}_{-0.8}$	65.3%
Wide Central	$0.57^{+0.33}_{-0.29}$	$13.6^{+8.3}_{-6.9}$	$6.8^{+0.8}_{-1.8}$	$3.2^{+0.7}_{-0.8}$	$5.0^{+1.0}_{-1.0}$	62.6%

Note. P_{bulge} is the probability of a lens in the Galactic bulge.

Table 5
Lensing Parameters with only the Survey Data

Parameters	2L1S				1L2S
	Central		Resonant		
	Close	Wide	Close	Wide	
χ^2/dof	2148.0/2156	2149.0/2156	2151.4/2156	2151.3/2156	2162.4/2156
$t_{0,1} - 10138$ (HJD′)	0.738 ± 0.001	0.738 ± 0.001	0.738 ± 0.001	0.738 ± 0.001	0.743 ± 0.002
$t_{0,2} - 10138$ (HJD′)	...	...	...	...	0.227 ± 0.016
$u_{0,1}(10^{-2})$	1.22 ± 0.02	1.22 ± 0.02	1.24 ± 0.02	1.23 ± 0.02	1.22 ± 0.01
$u_{0,2}(10^{-2})$	...	...	...	...	0.01 ± 0.13
t_E (days)	30.5 ± 0.4	30.5 ± 0.4	30.4 ± 0.4	30.5 ± 0.4	30.8 ± 0.4
$\rho_1(10^{-3})$	<3.5	<3.5	<3.6	<4.0	...
$\rho_2(10^{-3})$	...	...	...	...	$1.89^{+0.83}_{-0.74}$
α (degree)	216.47 ± 0.79	216.47 ± 0.80	216.54 ± 0.69	216.91 ± 0.87	...
s	0.886 ± 0.032	1.161 ± 0.039	0.986 ± 0.005	1.018 ± 0.003	...
$q(10^{-4})$	0.431 ± 0.134	0.439 ± 0.134	0.178 ± 0.035	0.227 ± 0.066	...
$\log q$	-4.387 ± 0.138	-4.378 ± 0.135	-4.757 ± 0.088	-4.662 ± 0.130	...
$q_{f,l}(10^{-3})$	...	...	...	...	3.35 ± 1.09
$I_{S,OGLE}$	18.756 ± 0.014	18.755 ± 0.014	18.752 ± 0.014	18.754 ± 0.014	18.768 ± 0.015

Note. The upper limit on ρ is 3σ ($\Delta\chi^2 = 9$).

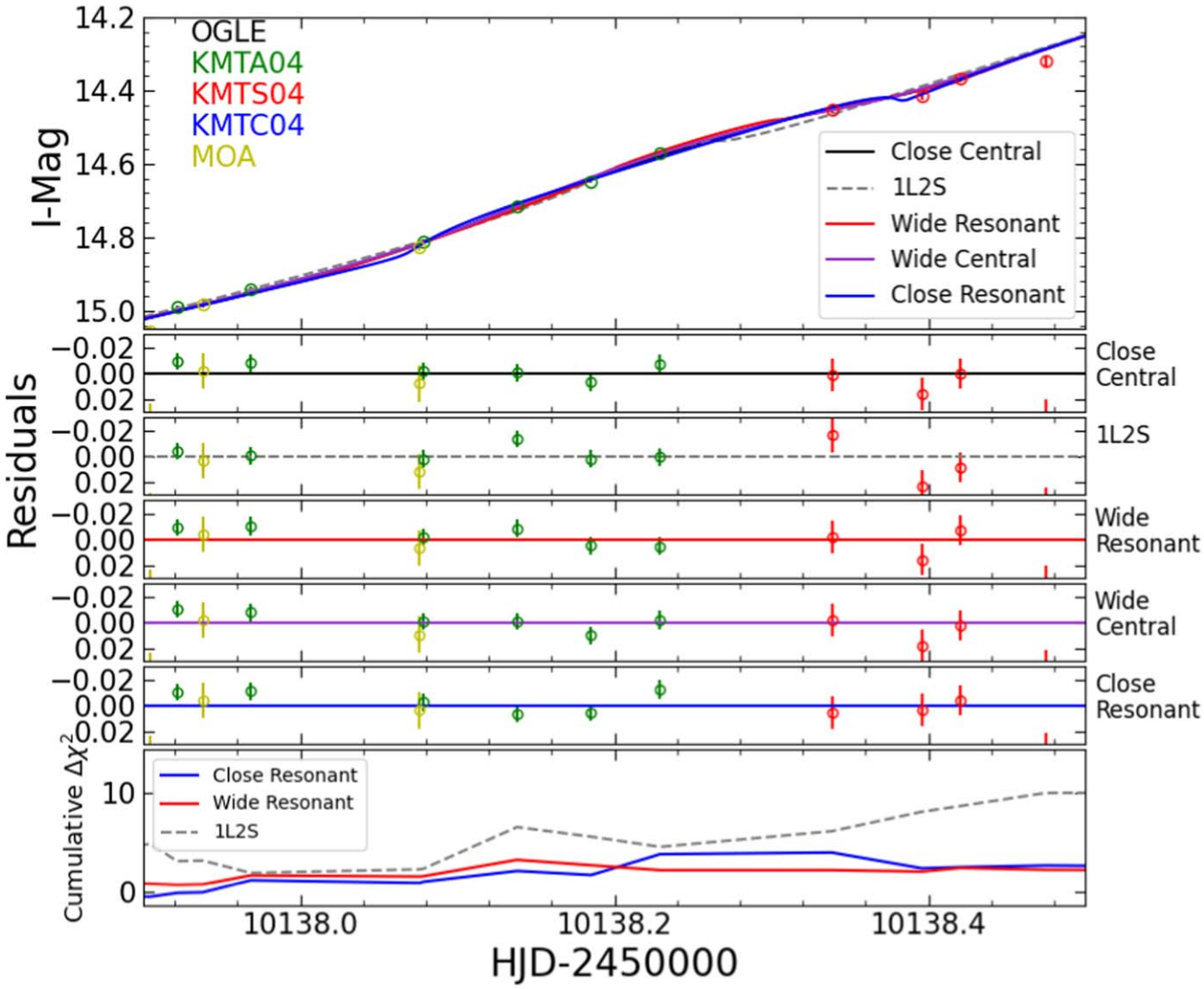

Figure 8. A close-up of the anomaly without the followup data and models fit to only the survey data.

"survey-only" case, we must remove the follow-up observations from LCO and FCO. We must also eliminate the extra KMTNet data that were taken in response to the alert.

Figure 8 shows the light curve in the anomaly region after removing these extra data points. Without the follow-up data, there are only a few points over the bump in the anomaly. In fact, the KMTNet AnomalyFinder algorithm (Zang et al. 2021b, 2022), which operates on the preliminary online pySIS data, on the survey-only KMTNet data cannot find the anomaly. The anomaly fails both the $\Delta\chi^2$ threshold and the requirement that "at least three successive points 2σ away from the PSPL model." So, without the follow-up data, this anomaly would not have been discovered by our automatic algorithm.

On the other hand, high-magnification events are often subject to increased by-eye scrutiny. So assuming that a person could identify the anomaly by eye, we can also ask how well it would be characterized by the survey data alone.

First, we consider whether or not it would be considered a robust detection, and we find $\Delta\chi^2 = 86.7$ for the best-fit 2L1S model relative to the PSPL model. Although planet detections at this low significance have been published, they tend to be negative perturbations rather than positive ones, because dips in the light curve are considered more robust to correlated noise (cf. OGLE-2018-BLG-0677 with $\Delta\chi^2 = 46$; Herrera-Martín et al. 2020). MOA-2010-BLG-311 serves as a counter example: at $\Delta\chi^2 \sim 80$, the anomaly was not considered robust enough to claim a detection (Yee et al. 2013).

Finally, even if the anomaly were considered detected in survey-only data, it would prove difficult to characterize. We repeated the model fits to the survey-only TLC data. The results are given in Table 5. This shows that, in the survey-only data,

the 1L2S model is only disfavored by $\Delta\chi^2 = 14$, which is marginally excluded, at best. Furthermore, the central/resonant degeneracy cannot be broken, with a maximum $\Delta\chi^2 \sim 3$ between the four solutions.

In conclusion, our follow-up data play an essential role in both the detection and characterization of this planetary anomaly. This planet, with $q = 0.7 \times 10^{-4}$, is a perfect example of the class of planets targeted by our systematic follow-up program, and it clearly demonstrates the continued need for such observations, even in the era of wide-field, high-cadence surveys.

Acknowledgments

We appreciate the anonymous referee for helping to improve the paper. W.Z. acknowledges the support from the Harvard-Smithsonian Center for Astrophysics through the CfA Fellowship. J.Z., W.Z., H.Y., S.M., S.D., Z.L., and W.Z. acknowledge support by the National Natural Science Foundation of China (grant No. 12133005). The SAO REU program is funded in part by the National Science Foundation REU and Department of Defense ASSURE programs under NSF grant no. AST-2050813, and by the Smithsonian Institution. Work by J.C.Y. and I.-G.S. acknowledge support from N.S.F grant No. AST-2108414. This research has made use of the KMTNet system operated by the Korea Astronomy and Space Science Institute (KASI) and the data were obtained at three host sites of CTIO in Chile, SAAO in South Africa, and SSO in Australia. Data transfer from the host site to KASI was supported by the Korea Research Environment Open NETwork (KREONET). This research was supported by the Korea Astronomy and Space Science Institute under the R&D program (Project No. 2023-1-832-03) supervised by the Ministry of Science and ICT. This research uses data obtained through the Telescope Access Program (TAP), which has been funded by the TAP member institutes. This work makes use of observations from the Las Cumbres Observatory global telescope network. The MOA project is supported by JSPS KAKENHI grant Number JSPS24253004, JSPS26247023, JSPS23340064, JSPS15H00781, JP16H06287, and JP17H02871. Work by R.P. and J.S. was supported by Polish National Agency for Academic Exchange grant "Polish Returns 2019." Work by C.H. was supported by the grants of National Research Foundation of Korea (2019R1A2C2085965 and 2020R1A4A2002885). Y.S. acknowledges support from BSF grant No. 2020740. The authors acknowledge the Tsinghua Astrophysics High-Performance Computing platform at Tsinghua University for providing computational and data storage resources that have contributed to the research results reported within this paper.

Software: pySIS (Albrow et al. 2009; Yang et al. 2024), MOA DIA pipeline (Bond et al. 2001), OGLE DIA pipeline (Wozniak 2000), numpy (Harris et al. 2020), emcee (Goodman & Weare 2010; Foreman-Mackey et al. 2013), Matplotlib (Hunter 2007), SciPy (Virtanen et al. 2020).

ORCID iDs

Aislyn Bell https://orcid.org/0000-0003-1946-4852
Jiyuan Zhang https://orcid.org/0000-0002-1279-0666
Weicheng Zang https://orcid.org/0000-0001-6000-3463
Jennifer C. Yee https://orcid.org/0000-0001-9481-7123
Hongjing Yang https://orcid.org/0000-0003-0626-8465
Andrzej Udalski https://orcid.org/0000-0001-5207-5619
Sang-Mok Cha https://orcid.org/0000-0002-7511-2950
Leandro de Almeida https://orcid.org/0000-0001-8179-1147
Richard Barry https://orcid.org/0000-0003-4916-0892
Przemek Mróz https://orcid.org/0000-0001-7016-1692
Jan Skowron https://orcid.org/0000-0002-2335-1730
Radoslaw Poleski https://orcid.org/0000-0002-9245-6368
Michał K. Szymański https://orcid.org/0000-0002-0548-8995
Igor Soszyński https://orcid.org/0000-0002-7777-0842
Paweł Pietrukowicz https://orcid.org/0000-0002-2339-5899
Szymon Kozłowski https://orcid.org/0000-0003-4084-880X
Krzysztof Ulaczyk https://orcid.org/0000-0001-6364-408X
Krzysztof A. Rybicki https://orcid.org/0000-0002-9326-9329
Patryk Iwanek https://orcid.org/0000-0002-6212-7221
Marcin Wrona https://orcid.org/0000-0002-3051-274X
Mariusz Gromadzki https://orcid.org/0000-0002-1650-1518

References

Abe, F., Airey, C., Barnard, E., et al. 2013, MNRAS, 431, 2975
Adams, A. D., Boyajian, T. S., & von Braun, K. 2018, MNRAS, 473, 3608
Alard, C., & Lupton, R. H. 1998, ApJ, 503, 325
Albrow, M. D., Horne, K., Bramich, D. M., et al. 2009, MNRAS, 397, 2099
An, J. H., Albrow, M. D., Beaulieu, J.-P., et al. 2002, ApJ, 572, 521
Bennett, D. P., & Rhie, S. H. 1996, ApJ, 472, 660
Bennett, D. P., Rhie, S. H., Nikolaev, S., et al. 2010, ApJ, 713, 837
Bensby, T., Yee, J. C., Feltzing, S., et al. 2013, A&A, 549, A147
Bessell, M. S., & Brett, J. M. 1988, PASP, 100, 1134
Bond, I. A., Abe, F., Dodd, R. J., et al. 2001, MNRAS, 327, 868
Bond, I. A., Bennett, D. P., Sumi, T., et al. 2017, MNRAS, 469, 2434
Bozza, V. 2010, MNRAS, 408, 2188
Bozza, V., Bachelet, E., Bartolić, F., et al. 2018, MNRAS, 479, 5157
Brown, T. M., Baliber, N., Bianco, F. B., et al. 2013, PASP, 125, 1031
Claret, A., & Bloemen, S. 2011, A&A, 529, A75
Dominik, M. 1999, A&A, 349, 108
Dong, S., Gould, A., Udalski, A., et al. 2009, ApJ, 695, 970
Einstein, A. 1936, Sci, 84, 506
Foreman-Mackey, D., Hogg, D. W., Lang, D., & Goodman, J. 2013, PASP, 125, 306
Gaudi, B. S. 1998, ApJ, 506, 533
Gaudi, B. S. 2012, ARA&A, 50, 411
Gaudi, B. S., Bennett, D. P., Udalski, A., et al. 2008, Sci, 319, 927
Goodman, J., & Weare, J. 2010, CAMCS, 5, 65
Gould, A. 1992, ApJ, 392, 442
Gould, A. 2000, ApJ, 542, 785
Gould, A. 2022, arXiv:2209.12501
Gould, A., & Loeb, A. 1992, ApJ, 396, 104
Gould, A., Shvartzvald, Y., Zhang, J., et al. 2023, AJ, 166, 145
Gould, A., Dong, S., Gaudi, B. S., et al. 2010, ApJ, 720, 1073
Griest, K., & Safizadeh, N. 1998, ApJ, 500, 37
Han, C., Udalski, A., Choi, J. Y., et al. 2013, ApJL, 762, L28
Han, C., Bennett, D. P., Udalski, A., et al. 2019, AJ, 158, 114
Han, C., Udalski, A., Lee, C.-U., et al. 2022a, A&A, 658, A93

Han, C., Gould, A., Bond, I. A., et al. 2022b, A&A, 662, A70
Han, C., Bond, I. A., Yee, J. C., et al. 2022c, A&A, 658, A94
Han, C., Zang, W., Jung, Y. K., et al. 2023a, A&A, 678, A101
Han, C., Lee, C.-U., Zang, W., et al. 2023b, A&A, 674, A90
Harris, C. R., Millman, K. J., van der Walt, S. J., et al. 2020, Natur, 585, 357
Herrera-Martín, A., Albrow, M. D., Udalski, A., et al. 2020, AJ, 159, 256
Hunter, J. D. 2007, CSE, 9, 90
Hwang, K.-H., Choi, J.-Y., Bond, I. A., et al. 2013, ApJ, 778, 55
Jung, Y. K., Zang, W., Han, C., et al. 2022, AJ, 164, 262
Jung, Y. K., Zang, W., Wang, H., et al. 2023, AJ, 165, 226
Kim, D.-J., Kim, H.-W., Hwang, K.-H., et al. 2018a, AJ, 155, 76
Kim, H.-W., Hwang, K.-H., Shvartzvald, Y., et al. 2018b, arXiv:1806.07545
Kim, S.-L., Lee, C.-U., Park, B.-G., et al. 2016, JKAS, 49, 37
Kroupa, P. 2001, MNRAS, 322, 231
Mao, S. 2012, RAA, 12, 947
Mao, S., & Paczynski, B. 1991, ApJL, 374, L37
Mayor, M., & Queloz, D. 1995, Natur, 378, 355
Mróz, P., Udalski, A., Skowron, J., et al. 2019, ApJS, 244, 29
Nataf, D. M., Gould, A., Fouqué, P., et al. 2013, ApJ, 769, 88
Olmschenk, G., Bennett, D. P., Bond, I. A., et al. 2023, AJ, 165, 175
Paczyński, B. 1986, ApJ, 304, 1
Ryu, Y.-H., Kil Jung, Y., Yang, H., et al. 2022, AJ, 164, 180
Sako, T., Sekiguchi, T., Sasaki, M., et al. 2008, ExA, 22, 51
Shin, I.-G., Yee, J. C., Gould, A., et al. 2023, AJ, 165, 8
Shvartzvald, Y., Yee, J. C., Calchi Novati, S., et al. 2017, ApJL, 840, L3
Sumi, T., Bennett, D. P., Bond, I. A., et al. 2013, ApJ, 778, 150
Suzuki, D., Bennett, D. P., Sumi, T., et al. 2016, ApJ, 833, 145
Szymański, M. K., Udalski, A., Soszyński, I., et al. 2011, AcA, 61, 83
Tomaney, A. B., & Crotts, A. P. S. 1996, AJ, 112, 2872
Udalski, A., Szymański, M. K., & Szymański, G. 2015, AcA, 65, 1
Udalski, A., Jaroszyński, M., Paczyński, B., et al. 2005, ApJL, 628, L109
Virtanen, P., Gommers, R., Oliphant, T. E., et al. 2020, NatMe, 17, 261
Wozniak, P. R. 2000, AcA, 50, 421
Yang, H., Mao, S., Zang, W., & Zhang, X. 2021, MNRAS, 502, 5631
Yang, H., Zang, W., Gould, A., et al. 2022, MNRAS, 516, 1894
Yang, H., Yee, J. C., Hwang, K.-H., et al. 2024, MNRAS, 528, 11
Yee, J. C., Shvartzvald, Y., Gal-Yam, A., et al. 2012, ApJ, 755, 102
Yee, J. C., Hung, L. W., Bond, I. A., et al. 2013, ApJ, 769, 77
Yee, J. C., Zang, W., Udalski, A., et al. 2021, AJ, 162, 180
Zang, W., Han, C., Kondo, I., et al. 2021a, RAA, 21, 239
Zang, W., Hwang, K.-H., Udalski, A., et al. 2021b, AJ, 162, 163
Zang, W., Yang, H., Han, C., et al. 2022, MNRAS, 515, 928
Zhang, J., Zang, W., Jung, Y. K., et al. 2023, MNRAS, 522, 6055
Zhu, W., Udalski, A., Calchi Novati, S., et al. 2017, AJ, 154, 210